NANO · MICRO small
www.small-journal.com

3D Confinement Stabilizes the Metastable Amorphous State of Antimony Nanoparticles – A New Material for Miniaturized Phase Change Memories?

Anne Frommelius, Konstantin Wirth, Thorsten Ohlerth, Dario Siebenkotten, Simon Wintersteller, Ahed Abouserie, Hongchu Du, Joachim Mayer, Maksym Yarema, Thomas Taubner, and Ulrich Simon**

The wet-chemical synthesis of 3D confined antimony nanoparticles (Sb-NP) at low and high temperatures is described. Using reaction conditions that are mild in temperature and strong in reducing power allows the synthesis of amorphous Sb-NP stabilized with organic ligands. Exchanging the organic ligand 1-octanethiol by iodide enabled to investigate the unusual strong stability of this metastable material through simultaneous thermal analysis combining differential scanning calorimetry and thermogravimetric analysis. Additionally, in situ high temperature powder x-ray diffraction (p-XRD) shows a significant increase in stabilization of the amorphous phase in comparison to thin layered, 1D confined Sb or bulk material. Further, it is shown with scattering-type scanning near-field optical microscopy (s-SNOM) experiments that the optical response of the different phases in Sb-NP make the distinctness of each phase possible. It is proposed that the Sb-NP introduced here can serve as a 3D-confined optically addressable nanomaterial of miniaturized phase change memory devices.

1. Introduction

Modern neuromorphic electronics for mobile, artificial intelligence,[1,2] or big data applications[3,4] generate an increasing demand for novel, non-volatile data storage devices.[5,6] One of the most promising and likewise mature technologies are phase change memories, that utilize the reversible switching between the crystalline and amorphous state of a phase change material (PCM) by electrical or optical means.[7–9] Among these materials, typically ternary compounds like $Ge_2Sb_2Te_5$, are employed, which require distinct stoichiometry and purity for proper function.[10–12] This however, sets limitations in cycling stability, as such complex compounds or alloys may undergo compositional partitioning during long-term use.[13–15] In order to overcome such stability limitations that arise from the materials' complexity, recently Salinga et al. reported a remarkable finding for pure Sb, when it is melt-quenched as a sub-10 nm layer between thermally and electrically insulating SiO_2 layers. It can be maintained in the amorphous state for up to 50 h, although it is known from textbooks of inorganic chemistry that amorphous Sb is metastable and tends to crystallize spontaneously already above 0 °C.[16,17] The authors found that the crystallization kinetics of the one dimensionally-confined amorphous antimony (Sb_{amo})

A. Frommelius, T. Ohlerth, A. Abouserie, U. Simon
Institute for Inorganic Chemistry
RWTH Aachen University
52074 Aachen, Germany
E-mail: anne.frommelius@ac.rwth-aachen.de;
ulrich.simon@ac.rwth-aachen.de

K. Wirth, D. Siebenkotten, T. Taubner
Institute of Experimental Physics
RWTH Aachen University
52074 Aachen, Germany

S. Wintersteller, M. Yarema
Institute for Electronics
ETH Zürich
Zürich 8092, Switzerland

H. Du, J. Mayer
Ernst Ruska-Centre for Microscopy and Spectroscopy with Electrons
Forschungszentrum Jülich GmbH
Central Facility for Electron Microscopy
RWTH Aachen University and JARA – Fundamentals of Future Information Technologies
52425 Jülich, Germany

The ORCID identification number(s) for the author(s) of this article can be found under https://doi.org/10.1002/smll.202402257

DOI: 10.1002/smll.202402257

decreased with decreasing thickness between 10 and 3 nm. In another study, Guo et al. investigated the crystallization properties of 50 nm Sb films deposited on Si/SiO_2 substrates and found a crystallization temperature (T_c) of 147 °C when the films were heated by a pulse laser with a heating rate of 30 °C min^{-1}.[18] Recent investigations performed on thin layers of amorphous Sb, in a range of 3–6 nm, showed not only the possibility of reversible laser-induced switching[19] and the distinguishable optical contrasts in each phase[20] but also a strong temperature dependent crystallization behavior. Therefore, the T_c for amorphous Sb thin layers was found to vary for 3–6 nm thickness in a range of 260–100 °C, respectively.[21–23] Hence, the 1D confinement holds promise for a new generation of devices based on monatomic switching cells, where compositional partitioning can be excluded. Very recently, Shen et al. reported an ab initio molecular dynamics (AIMD) simulation study of the different crystallization tendencies of antimony in bulk and thin layers. They found a large structural dissimilarity in the near-surface region of thin layered antimony which suppresses the crystallization as it decreases the nucleation rate and improves thermal stability.[24]

Therefore, it would be interesting to explore, whether a 3D confinement of Sb in the sub-10 nm range can lead to an even further stabilization of the metastable amorphous state in order to make Sb accessible for miniaturized phase change memory devices. The 3D-confinement is realized by the formation of colloidal nanoparticles (NP) in the respective size-range as they show a large surface/volume ratio the number of near-surface atoms is enlarged and could lead to even further thermal stability of the amorphous state. They would therein enable the analysis of fundamental aspects, such as the size dependent crystallization.

Beyond that, application-oriented studies on the size dependent optical and electrical switching on the single particle level would be of high interest.[25] Electrical switching experiments on individual chemically synthesized Sb_2Te_3 particles have been performed and therein limitations in the phase change cyclability became evident, which were attributed to structural degradation due to the depletion of tellurium.[26] This fundamental and well-known stability limitation could be overcome in a monoelemental material. Furthermore, the question arises whether other pnictogens (i.e., the more metallic Bi or the less metallic As) exhibit similar size-dependent properties. This would require a new synthetic approach for colloidal Sb, Bi, and As at individual temperatures in order to synthesize and isolate ligand stabilized NP in the metastable amorphous state.

Previously, the synthesis of colloidal amorphous and crystalline PCM NP was introduced. The NP consisted of GeTe and were formed via an amide-promoted approach in order to control the NP sizes.[27] It was found that T_c of amorphous GeTe-NP increases with decreasing particles size as a consequence of the confinement. In more detail, NPs of smaller diameter require a higher specific nucleation density, thereby exhibiting an increased T_c.[28] In comparison with bulk GeTe (T_c = 170 °C), the crystallization occurred at temperatures above 200 °C at particle sizes below 8 nm. We therefore hypothesize that a 3D-confinement can further stabilize the amorphous state of Sb, accordingly. There are only a few reports in the literature until now on the synthesis of colloidal Sb-NP. To give an example, He et al. reported the synthesis of crystalline colloidal sub-20 nm Sb-NP via a hot-injection approach. In this reaction, the usage of lithium diisoproylamide (LDA) activated oleylamine (Li-OAm) as ligand and reducing agent above 140 °C is crucial for the formation of these colloidal NP while at lower temperatures no particle formation occurred.[29] Further investigations on the synthesis of crystalline Sb-NP in size ranges of ≈15 and 35 nm are shown by Boebinger et al. adapting the hot-injection approach by He et al. with longer growing times and usage of different reducing conditions.[30] Balan et al. reported the formation of Sb_{amo}-NP embedded in a not further defined organic matrix by using *t*-BuONa-activated NaH as reducing and stabilization agent.[31] They concluded that these particles revealed first features of crystallization after thermal treatment at 160 °C, which approaches the anticipated T_c of Sb observed in the 50 nm films.[18] However, neither attempts to disperse individual particles in a solvent, which would allow for chemical processing of individual particles, nor thermal stability studies on such particles were performed. To the best of our knowledge, the synthesis of colloidal Sb_{amo}-NP in the relevant size range has not been reported yet. Particularly, the observed stabilization of amorphous Sb by 1D-confinement below the 10 nm threshold emphasizes the need to synthesize Sb-NP within the sub-10 nm range in order to take full advantage of 3D confinement.

In this work, we developed a synthetic strategy, which corresponds to the hot-injection approach, but which is performed to synthesize the Sb_{amo}-NP in a temperature range well below the anticipated T_c. This is enabled by combining trimethylsilylchloride (Me_3SiCl) and lithium boronhydride ($LiBH_4$) in THF with Li-OAm in order to generate a strongly reducing reaction environment. The formation of this unusually strong reducing conditions was first introduced by Giannis et al. who found that the reactive species is a BH_3·THF complex.[32] The structural features as well as the stability of these particles were analyzed via transmission electron microscopy (TEM) combined with electron diffraction (ED), powder X-ray diffraction (p-XRD) as well as in situ high-temperature p-XRD experiments and differential scanning calorimetry (DSC) combined with thermogravimetric analysis (TGA). Additionally, s-SNOM experiments were performed for an understanding of the optical properties of amorphous and crystalline antimony on the single particle level. Furthermore, the synthesis of bismuth (Bi-NP) and arsenic NP (As-NP) were performed at different temperatures to get information about possible stabilization of these materials in the metastable amorphous phases, as well. A schematic illustration of the performed synthesis can be found in **Figure 1**.

2. Results and Discussion

2.1. Synthesis of Crystalline and Amorphous Sb Nanoparticles

For the synthesis of the Sb-NP, first TOP was degassed in vacuo at 100 °C for 1 h before usage. Further, solutions of antimony(III)chloride ($SbCl_3$) in toluene (A), LDA in oleylamine (OAm) (B) and $LiBH_4$ combined with Me_3SiCl in THF (C) were prepared. Solution B and C were added to the reaction flask which led at high reaction-temperatures to a drop of the temperature of roughly 30 °C. After the reaction temperature was equilibrated, solution A was added in one shot which led to a formation of Sb-NP indicated by an immediate blackening of the reaction

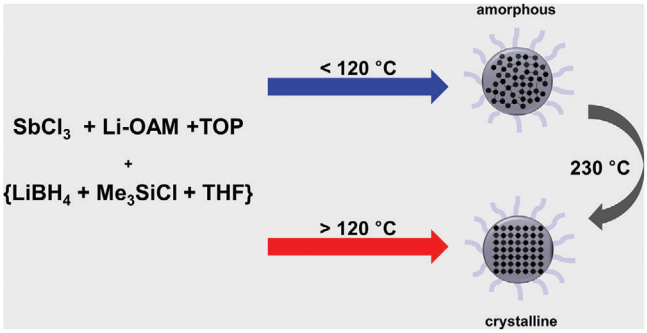

Figure 1. Schematic illustration of the performed synthesis to obtain Sb-NP in either crystalline or amorphous phase. Antimony(III)chloride ($SbCl_3$) is injected into a heated solution of Li-OAM and tri-*n*-octylphosphine (TOP). The addition of Me_3SiCl and $LiBH_4$ in THF allows the synthesis under mild temperature reaction conditions.

mixture. In order to avoid unintended agglomeration of Sb-NP the weakly binding ligand OAm was exchanged after purification of the achieved particles (see Experimental Section).[29,33] It should be noted that several potential ligands were tested in this ligand-exchange reaction, including pure OAm, dodecanoic acid, 1,2-diaminoethane, pyridine, and other similar organic molecules. Among these, the 1-octanethiol showed the highest stabilization and purity (for comparison TEM images of the Sb-NP with potential ligands can be found in Figure S1, Supporting Information). The as synthesized Sb-NP in crystalline and amorphous phase are shown in **Figure 2**. The synthesis of Sb-NP at temperatures above 120 °C led to roughly 9 nm sized crystalline particles in rhombohedral crystal structure, which was confirmed by ED and p-XRD in comparison to ICSD data.[34] In contrast, when the reaction was performed at room temperature, the formation of isolated particles resulted which are ≈8 nm in size. These particles were found to be amorphous, as derived from p-XRD and ED (Figure 2).

An additional overview of TEM images and corresponding ED as well as XRD measurements of the as-synthesized Sb-NP at different temperatures (160, 130, 60, and 40 °C) can be found in the supporting information (Figure S2, Supporting Information). Furthermore, the synthesis of As- and Bi-NP was done similarly at different temperatures using also halide-precursors. The as-synthesized particles were analyzed using TEM combined with ED as well as p-XRD measurements. For the As-NP, it could be seen that even at high reaction temperatures of 160 °C, the non-metallic As-NP could not be obtained in the crystalline phase (Figure S3, Supporting Information). Additionally, the amorphous As-NP were aged over 6 months under ambient temperature (≈30 °C) and measured in p-XRD again. It could be observed that even though the amount of oxygen was kept low due to the storage in an argon-filled container, the particles oxidized and formed As_2O_3 (Figure S3, Supporting Information).[35] The synthesis for Bi-NP in a huge variety of morphologies and sizes is already well-known in the literature.[36–38] In the as-described approach the formation of crystalline 4 nm-sized spherical Bi-NP was achieved. Due to its more metallic character, the Bi-NP could not be obtained in the amorphous phase even at reaction temperatures below 0 °C, which was proven as well by TEM combined with ED and p-XRD measurements (Figure S4, Supporting Information). An oxidation after several months of storage under similar conditions as for the Sb- and As-NP was not observed which reflects a stronger tendency to react with oxygen with decreasing atomic number among the group 15 elements. According to Kepp, this aligns well with the oxophilicities of Bi, Sb, and As, being 0.2, 0.3, and 0.5, respectively.[39] These values, which are deemed to correlate to electronegativity and effective nuclear charge, demonstrate the lowest oxygen affinity for bismuth. Additionally, examining the oxide formation enthalpies (ΔH_f) reveals that cubic Sb_2O_3 exhibits the highest exothermy with $\Delta H_f = -720.5$ kJ mol^{-1}, followed by As_2O_3 with $\Delta H_f = -657.4$ kJ mol^{-1} and Bi_2O_3 with $\Delta H_f = -573.9$ kJ mol^{-1}, which accords with the trend in oxophilicity.[17]

2.2. Thermal Investigations on Metastable 3D Confined Amorphous Sb-NP

2.2.1. Simultaneous Thermal Analysis

The crystallization behavior of Sb_{amo}-NP stabilized with 1-octanethiol ligand (@1OT) was first analyzed by simultaneous thermal analysis (STA) where DSC and TGA are performed concurrently. For the measurements, the NP were heated up with different rates up to 500 °C under constant nitrogen flow. In the first approach, the experiment was performed with Sb_{amo}-NP@1OT which showed an exothermic peak directly followed by two strong endothermic peaks most likely due to the evaporation of poorly as well as strongly adsorbed ligand molecules, respectively. Using different heating rates, we observed that all thermal phenomena were shifting towards higher temperatures with higher heating rates. The hypothesis that the endothermic peaks are related to the evaporation of organics is in good agreement with the two mass loss events seen at ≈250 °C and 300 °C for Sb_{amo}-NP@1OT heated with 5 °C min^{-1} rate (Figure S5A–C, Supporting Information). The broad exothermic peaks that were partially overlapping with the evaporation peaks of the ligand indicate the crystallization of the Sb_{amo}-NP at ≈230 °C for the heating rate of 5 °C min^{-1}. The DSC curve shows after the second endothermic peak an additional, very broad exothermic feature. This can most likely be attributed to the coalescence of the NP as the organic ligand is removed during the heating process. Furthermore, crystalline Sb-NP stabilized by 1OT showed similar behavior at temperatures above the evaporation of ligand molecules, supporting the assumed coalescence taking place (Figure S6B, Supporting Information). In order to get more precise information of these thermal phenomena the DSC experiments were performed again with Sb_{amo}-NP@I$^-$ to exclude endothermic peaks resulting from ligand release. The thermograms showed solely exothermic features that could only be observed in very low intensity, which shifted towards higher temperatures with increasing heating rates. Further, similarly to the 1OT stabilized Sb-NP a second broad exothermic peak at higher temperatures could be observed. The crystallization of the Sb_{amo}-NP@I$^-$ at 5 °C min^{-1} was assigned to $T_c = 171$ °C which in comparison to Sb_{amo}-NP@1OT decreased about roughly 60 °C (Figure S5D–F, Supporting Information). Similarly treated GeTe iodide stabilized NP showed that the coalescence starts prior to the crystallization while GeTe-NP with organic ligands crystallize first and coalesce afterward.[27]

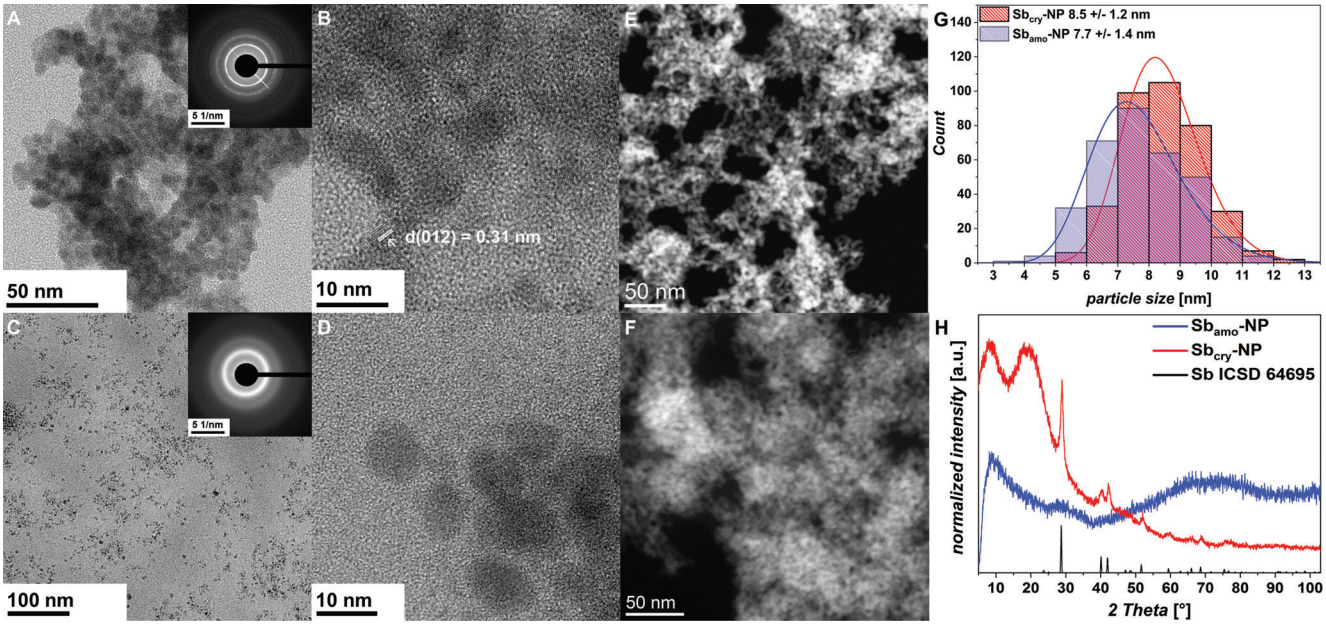

Figure 2. A) TEM image of crystalline Sb-NP with inserted ED pattern (top right) revealing a polycrystalline ring-pattern. B) High resolution TEM image of crystalline Sb-NP showing the lattice plane value d(012) = 0.31 nm. C) TEM image of Sb_{amo}-NP with inserted ED (top right) showing an amorphous ring pattern. D) High resolution TEM image of Sb-NP indicating the lack of crystallinity. E,F) STEM images of crystalline and amorphous Sb-NP, respectively. G) Size histogram for amorphous and crystalline Sb-NP revealing similar sizes of ≈8 and 9 nm in diameter, respectively. Images of particles used for estimated size-distribution can be found in Supporting Information. H) P-XRD of both amorphous and crystalline Sb-NP in comparison to ICSD data of rhombohedral Sb.[34]

The Sb-NP seems to behave differently as the I^- shows to have good stabilizing properties as the broad signal of coalescence occurs after the crystallization. In the case of GeTe, the stabilization with iodide is equated with ligand-free NP which apparently does not account for the Sb-NP@I^- as these show in DSC the coalescence occurring after the crystallization.[27]

Additionally, when the Sb_{amo}-NP were heated up to temperatures of 700 °C a sharp endothermic peak can be observed at ≈630 °C in respective of the stabilization by organic or inorganic ligand (Figure S6A, Supporting Information). This can be identified as the melting of antimony which is in good agreement with the T_m of the bulk, i.e., 630.6 °C. The fact that T_m is not significantly lower than of bulk Sb supports the assumption of already coalesced particles.[40] For both, organic and inorganic stabilized Sb_{amo}-NP, the identified T_c at different heating rates were used to estimate the activation energy E_a of crystallization for the Sb_{amo}-NP. We therefore apply the Kissinger Equation (1):[41]

$$E_a = R * \frac{\ln\left(\theta/T_p^2\right)}{1/T_p} \quad (1)$$

where R is the gas constant, T_p the temperature at the peak maximum, and θ the heating rate of the experiment. In order to obtain E_a in eV, the ideal gas constant is converted with the Avogadro constant and elementary charge times volt to get to the Boltzmann constant $k_B = 8.617 \cdot 10^{-5}$ K eV^{-1}. By this E_a was evaluated as the slope of the Kissinger plot of $\ln(\theta/T_p^2)$ versus $1/T_p$ multiplied by k_B (**Figure** 3A,B). For the Sb_{amo}-NP@1OT, E_a was estimated to be 2.24 ± 0.12 eV and for Sb_{amo}-NP@I^- to be 1.05 ± 0.20 eV. The higher activation energy of Sb_{amo}-NP@1OT in comparison to Sb_{amo}-NP@I^- might tentatively be explained by the different binding of the thiol-group forming a robust metal-thiol coordination bond as it is known for a ligand-nanoparticle system[42] while the iodide ions stabilize the NP through electrostatic interactions.

Salinga et al. calculated E_a values for the crystallization of 3–10 nm thin layered amorphous Sb to be in a range of 1.0–1.3 eV[16] which is in a similar scale as 3D-confined Sb_{amo}-NP@I^-. While the energy barrier to crystallize Sb_{amo}-NP@1OT is quite larger with 2.2 eV and more similar to that of amorphous GeTe-NP calculated to 3.3 eV.[27] This grading of 3D-confined amorphous Sb in comparison to similar PCM gives great opportunities to investigate its applicability in data memory devices. As the exothermic peaks in DSC were either overlapped by the evaporation of organics or showed low intensity the assigned crystallization of the Sb_{amo}-NP was validated by high-temperature in situ XRD measurements.

2.2.2. X-Ray Diffraction

In order to probe the (long-term) stability of 3D-confined Sb_{amo}-NP against crystallization, first the particles were stored under argon at room temperature and were measured by p-XRD once a week over a time span of 9 weeks (Figure S7C, Supporting Information). Herein, Bragg reflections were observed after 6 weeks, reflecting a tremendous increase in stability of the amorphous nanoparticulate phase in comparison to thin layers or bulk material.[16,17] To further analyze the stability of Sb_{amo}-NP

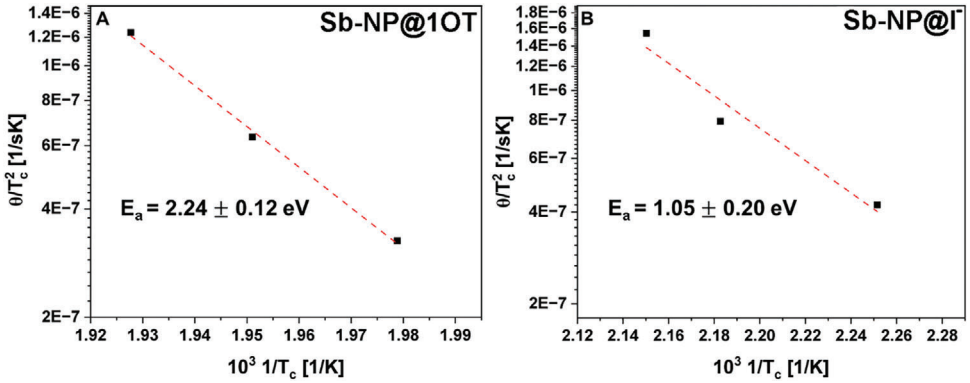

Figure 3. T_c of Sb_{amo}-NP heated with different heating rates are shown in a Kissinger plot showing Arrhenius-like behavior. The activation energy for organic ligand stabilized particles was calculated to $E_a = 2.24 \pm 0.12$ eV A). For the inorganic ligand stabilized Sb_{amo}-NP the activation energy showed an activation energy for the crystallization of $E_a = 1.05 \pm 0.20$ eV B).

against crystallization we measured the particles with in situ high-temperature p-XRD to observe heat-induced crystallization features. Therefore, the two particle types Sb_{amo}-NP@1OT and Sb_{amo}-NP@I$^-$ were heated up to 400 °C with a heating ramp of 4 °C min^{-1} where diffraction was measured at each heating step. In **Figure 4**A a heat profile of the crystallization of Sb_{amo}-NP@1OT is illustrated where two crystallization features can be identified occurring at a temperature of ≈230 °C. These reflections can be assigned to cubic Sb_2O_3 at 27.7° 2θ and rhombohedral Sb at 28.7° 2θ. Even though all preparation steps were performed under inert conditions the formation of Sb_2O_3 could not be prevented due to the high tendency of Sb to form oxides. However, both phases remain stable up to 400 °C suggesting that Sb_{amo}-NP@1OT are not fully oxidized and could still show potential as a PCM. This is especially important since they have a much higher T_c than the aforementioned non-3D-confined Sb, suggesting improved data retention performance. In the case of Sb_{amo}-NP@I$^-$, the first visible crystallization feature at 28.7° 2θ can be identified at ≈160 °C which is roughly 70 °C lower than in the case of Sb-NP@1OT and can be assigned to rhombohedral Sb (Figure 4B). Even though the crystallization of Sb_{amo}-NP@I$^-$ occurs at a much lower temperature a second crystal feature from the formation of Sb_2O_3 does not occur. Despite the fact that all chemicals used prior to the ligand exchange are identical and purified/distilled before usage (see Experimental Section) unintended oxygen contamination seems not to be fully avoided.

A tentative explanation for the apparent oxidation stability of Sb-NP@I$^-$ could be that the iodide ions are more densely packed on the surface of the NP and therefore kinetically hinder the reaction with oxygen. Another assumption is that surface oxidation is prevented because an excess of iodide leads to the formation of a protective capping phase, $Sb_xO_yI_z$, on the particle surface.[44] This kind of passivating layer could hinder the formation of Sb_2O_3. In order to get more insights on this manner, XPS measurements of Sb-NP stabilized by organic and inorganic ligands were performed giving the Sb 3d spectrum with characteristic peaks of Sb^0 and Sb^{3+} showing the typical doublet separation for Sb $3d_{5/2-3d_{3/2}}$: 9.38 ± 0.08 eV due to spin orbit coupling (**Figure 5**).[45,46] The binding energies for Sb-NP@I$^-$ found as shoulder peaks at 528.5 and 537.9 eV correspond to the $3d_{5/2}$ and $3d_{3/2}$ of Sb^0, respectively.[47] Additionally, the two sharp peaks at 530.4 and 539.7 eV can be identified as $3d_{5/2}$ and $3d_{3/2}$ of a Sb^{3+} species. The

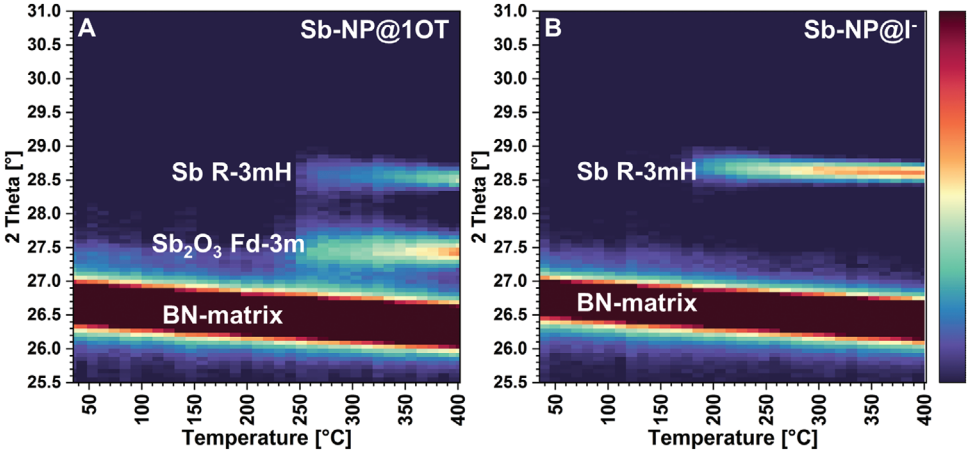

Figure 4. Heat map of in situ HT p-XRD measurement of Sb-NP_{amo}-NP stabilized by 1OT where first crystallinity can be estimated to ≈230 °C A) and by inorganic ligand I$^-$ where first crystallinity is visible at ≈160 °C B) measured in a BN matrix. The reference data used for Sb and Sb_2O_3 stems from ICSD.[34,43] The reflection of BN matrix was identified by measuring the material without Sb sample.

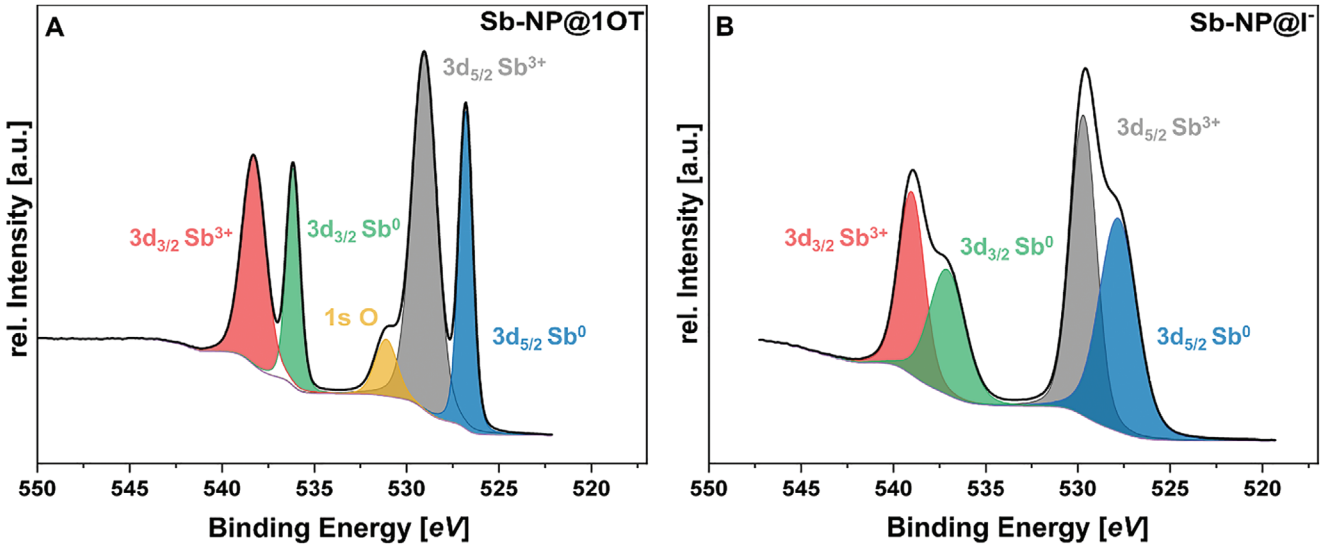

Figure 5. XPS measurement of the Sb 3d spectrum in Sb-NP@1OT A) and Sb-NP@I^- B) for clearer identification the binding energies are assigned to the individual 3d state. 1OT stabilized particles show next to the 3d spectrum of Sb also 1s of oxygen which cannot be identified for the iodide stabilized Sb-NP.

binding energy for Sb^{3+} in compound SbI_3 and Sb_2O_3 only differs by 0.1 eV, nevertheless, a formation of an oxidized species can be ruled out even though the sample preparation was performed under ambient air due to the fact that no peak for the binding energy of the 1s corresponding to oxygen at 531.4 eV can be identified (Figure 5B). In comparison the Sb-NP@1OT shows next to the $3d_{3/2}$ and $3d_{5/2}$ signals from Sb an overlapping signal at 532.3 eV which can be identified as the 1s of oxygen (Figure 5A). Furthermore, the 3d spectrum of iodine could be identified for Sb-NP@I^- however, discerning whether it originates from free ions or a formed passivating layer appears to be unattainable due to the limitations in quantification.

Therefore, pure SbI_3 was measured in XPS as well to compare the binding energies with the iodide stabilized particles (Figure S8B, Supporting Information). At this point, a precise explanation for the stabilization of Sb-NP against oxidation by the iodide ligand remains elusive. Further XPS measurements, show the success of the ligand exchange where in Sb-NP@I^- only a very small residue of sulfur was detected in comparison to Sb-NP@1OT (Figure S8, Supporting Information).

2.2.3. Optical Response of Amorphous and Crystalline Sb Nanoparticles

Sb is a PCM upon confinement in at least one dimension that shows a substantially higher resistance in the amorphous compared to the crystalline phase.[16] Thus, we also expect a higher charge carrier density in the crystalline state.[7] The free charge carriers will have a more pronounced influence on the infrared permittivity in the crystalline than in the amorphous phase.[48] By combining these argumentations, we expect for crystalline Sb a free charge carrier dominated permittivity and for amorphous state Sb a suppressed Drude contribution, and thus positive permittivity.

The permittivity of bulk Sb and for films down to 27 nm thickness is reported to have a free charge carrier induced Drude-like zero-crossing ≈900 cm^{-1}.[49] The investigated films in these reports are crystalline, as antimony is prone to crystallization.[16] In contrast to bulk materials, the permittivity of the NP is also influenced by confinement effects[50] and localized plasmon resonance (LSPR) of individual NP.[51]

Optical measurements of large ensembles of NP are possible with conventional optics for example with Fourier transform infrared spectroscopy (FTIR) or Raman scattering. Due to the optical diffraction limit, conventional spectroscopic techniques lack the lateral resolution desired for the investigation of optical properties of structures below half of the incident wavelengths, such as individual NP. The diffraction limit in resolution can be overcome by employing infrared s-SNOM. Here, light scattered at a sharp tip is used to record the optical properties of the sample via its permittivity.[52] The lateral resolution in s-SNOM is determined by the radius of the tip apex. Thus, a lateral resolution down to 20 nm can be achieved at infrared frequencies.[53]

The permittivity-dependent s-SNOM contrast is explained in Figure S9 (Supporting Information). S-SNOM has been used to determine the different optical response of NP in the single-digit nanometer regime, for example for the distinction of polystyrene ($\varepsilon_{PS} = 2.4 + 0.1i$) and Au-NP ($\varepsilon_{AU} = -500 + 1000i$) down to 5 nm in diameter[54,55] or of sub-tip radius proteins.[56]

In **Figure 6A** the working principle of these measurements is depicted. For NP sizes in the order of the tip radius, the field enhancement, which decays exponentially away from the s-SNOM tip, probes both the substrate and the NP. This coupled tip-NP-substrate system changes the s-SNOM scattering amplitude, depending both on the size and permittivity (amorphous/crystalline) of the NP; and distance and dielectric properties of the substrate. For very small NP sizes, the distance between tip and substrate increases which leads to a decreasing s-SNOM amplitude (green area in Figure 6A). The coupling of

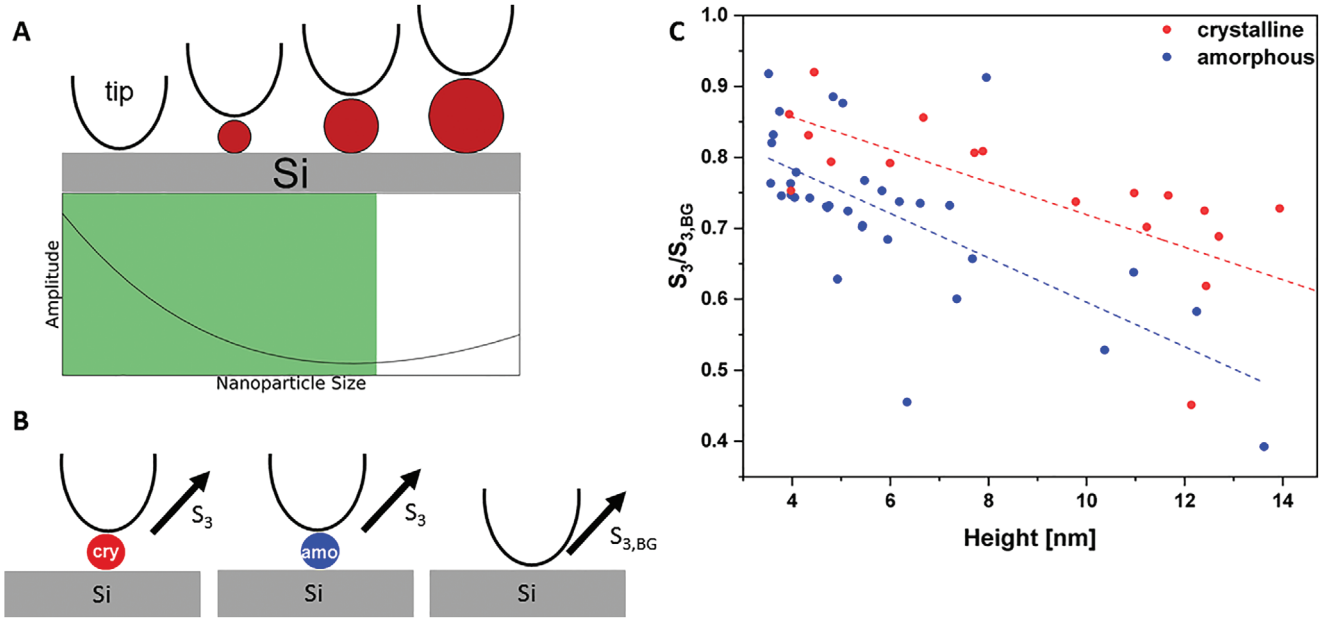

Figure 6. A) Schematic illustration of s-SNOM probing of individually differently sized NP (red spheres). Bottom: expected scaling behavior of scattering amplitude (relevant regime marked in green): For increasing NP size, the s-SNOM amplitude is expected to decrease in a characteristic way depending on the NP optical properties. B) Sb-NP in either crystalline or amorphous state on a silicon wafer with the s-SNOM tip and the scattered light indicated. C) Normalized s-SNOM scattering amplitude $\tilde{S}_3 = S_3/S_{3,BG}$ taken at 900 cm^{-1} on top of crystalline (red) and amorphous Sb-NP (blue) plotted against their size (taken from the topographical height). $S_{3,BG}$ corresponds to the amplitude on the surrounding silicon substrate. Each data point represents a single nanoparticle. The trend line is given as an optical assistant to showcase the different grading of the optical signal for both phases in different sizes.

the tip to the NP is weaker than the substrate coupling, but still causes a different decay behavior for different NP materials due to their polarizability $\alpha_p = 4\,\pi\, r(\varepsilon_p - 1)/(\varepsilon_p + 2)$, where r is the radius of the NP and ε_p the permittivity. For NP much larger than the tip radius (which we did not investigate here), the coupling to the NP would at some point dominate over the coupling to the substrate, leading to a s-SNOM amplitude increase with increasing NP size. In our case, the differences in s-SNOM amplitude for the amorphous/ crystalline Sb-NP can be related to their permittivity. A more in-depth explanation of the s-SNOM amplitude and the permittivity of the NP can be found in Figure S9 (Supporting Information).

As illustrated in Figure 6B the amorphous and crystalline Sb-NP were deposited on two silicon wafers and measured subsequently at 900 cm^{-1}. In Figure 6C the normalized s-SNOM amplitude $\tilde{S}_3 = S_3/S_{3,BG}$ extracted on top of individual Sb-NP is plotted against their diameter. The crystalline NP clearly show higher $\tilde{S}_3$ than the amorphous ones, thus a distinction via s-SNOM is in principle possible. The higher $\tilde{S}_3$ of crystalline compared to the amorphous Sb-NP indicates that the crystalline NP can better compensate for the weaker coupling between tip and substrate with increasing distance.[54] The theoretical analysis of the s-SNOM contrast in Figure S9 (Supporting Information) supports our conclusion that there is a significant difference in the permittivity between amorphous and crystalline NP. Following the theoretical analysis, we have two possible explanations for the experimentally observed difference in $\tilde{S}_3$ of the amorphous/crystalline Sb-NP at this point. First, the permittivity of the crystalline NP $\varepsilon_{cry} << 0$ could be more metallic/plasmonic with ε_{amo} being slightly negative. Second, $\varepsilon_{cry} >> 0$ and ε_{amo} could be close to 0. The higher $\tilde{S}_3$ for crystalline NP's $\tilde{S}_3$ compared to amorphous NP, indicates a rather plasmonic or metallic character of the crystalline NP and a dielectric one for the amorphous NP. This result is in good agreement with the expectations for the bulk case, that the permittivity of the crystalline Sb-NP is dominated by free charge carriers, whereas in amorphous Sb-NP the free charge carrier contribution is suppressed.

Our results lay the foundation for follow-up experiments involving the spectroscopic (frequency-dependent) investigation of Sb-NP to determine their resonance. In NP, the LSPR resonance is governed by the number of free charge carriers and the size of the NP. The number of free charge carriers could be directly linked to the charge carrier density and, thus, the number of defects in the NP. For example, in the NP size range investigated here, 10 to 100 free charge carriers per NP would correspond to a free charge carrier density of up to 10^{20} cm^{-3} and thus an LSPR in the mid-infrared regime.[52] In conclusion the stability of the 3D-confined amorphous antimony was validated in s-SNOM measurements as these were performed at room temperature As the amorphous phase is stable against crystallization over the cause of several weeks (see Figure S7, Supporting Information).

The differences in the permittivity for Sb-NP for both phases might be suitable for optically addressable memory devices.

3. Conclusion

The syntheses of 3D-confined antimony in form of amorphous and crystalline NP phase have been performed. By thermally

analyzing the Sb_{amo}-NP with organic ligands the evaporation of organics took place simultaneously with the crystallization of the amorphous Sb. Therefore, an exchange of ligands to inorganic iodide was performed and showed successful stabilization of the Sb-NP as well. The DSC measurements showed crystallization features of the inorganically stabilized at ≈70 °C lower temperatures than of organically stabilized Sb-NP. In both cases activation energies for the crystallization for the Sb_{amo}-NP was analyzed showing that Sb-NP@I^- with $E_a = 1.1$ eV is similar to the amorphized 5 nm thin layered Sb with $E_a = 1.0$ eV. While the Sb_{amo}-NP@1OT showed more increased thermal stability and an activation energy of $E_a = 2.2$ eV, which is much closer to conventionally used PCM as GeTe-NP ($E_a = 3.2$ eV). For 4 nm thin layered amorphous Sb an activation energy measured to be $E_a = 2.08$ eV which is quite similar to ≈8 nm sized Sb_{amo}-NP@1OT.[22] In future studies it would therefore be of great interest, to compare smaller-sized 3D confined Sb-NP to further investigate the improved stability of amorphous Sb. Additionally, in situ high-temperature p-XRD of both organically and inorganically stabilized Sb_{amo}-NP confirmed the crystallization of the particles at similar temperatures as found in DSC experiments. Herein, the organically stabilized Sb-NP showed a tendency to oxidize which appeared to be less pronounced when the surface was covered with small ions instead of large organic molecules. Even though the thermal stability against crystallization is higher when stabilized by organic molecules the stabilization with iodide improves the stabilization of Sb against oxidation. Furthermore, a difference in the normalized s-SNOM amplitude response $\tilde{S}_3$ was found between the amorphous and crystalline Sb-NP in s-SNOM experiments. The observed difference in $\tilde{S}_3$ indicates a more metallic permittivity for crystalline Sb-NP than for the amorphous ones.

These results make 3D-confined antimony a great candidate for future investigations in terms of laser-induced (reversible) switching experiments. Furthermore, spectroscopy on an individual NP level over a broad spectral range could be used to determine the optical properties of the NP via its permittivity and determine the influence of confinement effects[50] and localized plasmon resonance.[51]

Our findings lead us to the conclusion that the 3D-confinement of materials can have a strong impact on their properties and hence gives more possibilities for applications. Especially in the case of antimony as a monoelemental PCM where the size reduction does not come with degradation or compositional partitioning these findings could lead to the implementation of the 3D-confined Sb-NP in an optically addressable prototype of a phase change memory device.

4. Experimental Section

Synthesis of Crystalline and Amorphous Group 15 Nanoparticles: For the synthesis of the Sb-NP first tri-*n*-octylphosphine (TOP) was degassed in vacuo at 100 °C for 1 h before usage. Typically, 29 mg $SbCl_3$/39 mg $BiCl_3$/57 mg AsI_3 (0.125 mmol) were dissolved in 2 mL of toluene and 385 mg LDA (3.6 mmol) mixed with 2 mL OAm. The Li-OAm was kept in an ultrasonic bath for 20 min at temperatures of ≈30 °C for faster dissolution. Under counter-flowing argon TOP was heated in a three-necked Schlenk round-bottomed flask with a return condenser to the required reaction temperatures (160 °C down to −5 °C). The Li-OAm was added which led at high temperature-reactions to a drop of the temperature of roughly 30 °C. Additionally, a mixture of 35 mg $LiBH_4$ (1.6 mmol) in THF and 0.5 mL of Me_3SiCl (3.9 mmol) was added. After the reaction temperature was equilibrated the $SbCl_3$/$BiCl_3$/AsI_3 solution was added in one shot which led to a formation of Sb/Bi/As-NP indicated by an immediate blackening of the reaction mixture. After 10 s the mixture was cooled down with an ethanol/$N_{2(l)}$ bath (≤ − 70 °C). Additionally, 12 mL of 4 °C cold *n*-hexane were added to quench the reaction. Furthermore, the protocol of He et al. was followed and added 0.1 mL of 1-dodecanethiol in order to enhance the colloidal stability.[29] The mixture was let thaw and stirred at room temperature for 1 h. Remaining organic substances including excess reducing agent, ligand, and reaction side products, were removed by repeated (2–3 times) centrifugation at 2000 rpm for 10 min, precipitation in ethanol, and redispersion in tetrachloroethylene (TCE). In order to avoid unintended agglomeration of Sb-NP the weakly binding ligand OAm was exchanged afterward.[29,33] Therefore, 1 mL 1OT was added to the NP mixture and sonicated for 2 min. The particles were purified again as described before and stored in TCE under inert conditions. Prior to the investigation under TEM the NP were highly diluted and pressed through a 0.02 µm Whatman Anotop syringe filter in order to get rid of any agglomerated particles.

Ligand Exchange from Organic Molecules to Inorganic Ions: In order to exchange the 1OT ligand to iodide ions the Sb_{amo}-NP were precipitated by centrifugation at 8000 rpm min^{-1} for 5 min and dispersed in 500 µL toluene. The NP were layered on 5 mL of a 20 mg mL^{-1} solution of SbI_3 in DMF and 10 mL *n*-hexane to achieve a two-phase system in which the particles first were found in the *n*-hexane phase. The mixture was then vigorously shaken for ≈3 min and let thaw for roughly 1 h after which the particles diffused into the DMF phase. The Sb_{amo}-NP were washed 3 times with *n*-hexane and then precipitated and washed with chloroform by repeated centrifugation at 8000 rpm min^{-1} for 5 min with 5 mL chloroform.[27,57]

Materials: $SbCl_3$ purchased from abcr (99.999 %, ampouled). SbI_3 purchased from abcr (99.9 %). AsI_3 (99.9 %), $BiCl_3$ (>98 %), tri-*n*-octylphosphine (TOP, 97 %), lithium diisopropylamide (LDA, 97 %), lithium tetrahydroborate ($LiBH_4$, 95%), trimethylsilyl chloride (Me_3SiCl, 99%), boron nitride (BN, 98%), oleylamine (OAm, 90 %), and tetracholorethylene (TCE, anhydrous, >99 %) were purchased from Sigma Aldrich, Merck. TCE was degassed and stored in an argon-filled glovebox and OAm distilled 3 times until the texture of the white wax was hard at room temperature. Absolute ethanol was purchased from VWR, degassed, and stored under argon. THF, *n*-hexane, toluene, chloroform, and DMF were purchased from Honeywell and purified in a solvent pressure system and directly forwarded into an argon-filled glovebox.

(Scanning) Transmission Electron Microscopy: TEM measurements were performed at a Zeiss Libra 200 with an acceleration voltage of 200 kV. STEM measurements were performed with the FEI Titan G2 80–200 ChemiSTEM microscope equipped with a high-brightness Schottky field emission electron gun and a probe Cs corrector. The samples were prepared in an argon-filled glovebox. Therefore, the particles were highly diluted in the respective solvent (TCE or chloroform), pretreated with an ultrasonic finger with an amplitude of 25 % for at least 1 min and afterward quickly drop-casted onto a carbon-supported copper grid (200 mesh). For the transfer of the grid into the TEM short exposure to air could not be fully avoided.

Simultaneous Thermal Analysis: DSC combined with TGA was performed with the STA-PT1600 from Linseis. Heating conditions were changed from 5 to 10 and 20 °C min^{-1}. The samples were prepared inside an argon filled glovebox in order to prevent oxidation of the Sb-NP. The samples were precipitated with ethanol and centrifuged at 8000 rpm for 3 min and diluted in 500 µL chloroform. Hundred microliters of the sample was then put into an Al_2O_3 crucible and the solvent was slowly let dry in the vacuum chamber of the glovebox. This process was repeated 4 more times and a maximum weight of ≈2–5 mg in total achieved. The sample was then closed with an Al_2O_3 lid with a small hole in the middle and air tightly transferred to the STA device. The transfer from the air-tight vessel into the measurement device was not possible in an air free manner but kept as short as possible. The sealed measurement chamber was

evacuated 3 times and filled with pure nitrogen (5.0) and the measurement performed under a constant nitrogen flow of 80 sscm min^{-1}.

Powder X-Ray Diffractometry: The p-XRD analysis was performed on a STOE Stadi P powder diffractometer with a Cu-anode (40 kV, 30 mA) radiation source (Cu-K_α = 0.154 059 nm) for a 2θ range of 5 – 100° and were conducted for 2 h. For the measurements, the sample was in solution drop-casted onto an acetate foil and let dry inside of an argon-filled glovebox. The dried foil was then closed with a second foil impregnated with grease in order to prevent sample loss and immediate air contact.

High-Temperature X-Ray Diffraction: High-temperature p-XRD measurements were performed on a Rigaku SmartLab 9 kW System, equipped with rotating Cu anode and 2D solid state detector (HyPix-3000 SL) and high-temperature stage (Anton Paar). Measurements were performed using a parallel beam geometry with a step-size of 0.01° within a 2θ range of 26.5 – 30.7° and a scanning speed of 5 °/min. The sample preparation was constantly performed in a nitrogen-filled glovebox. The treatment of organic and inorganic ligand-stabilized Sb-NP was identical. The Sb_{amo}-NP were precipitated with ethanol and centrifuged at 8000 rpm for 3 min. The NP were then dissolved in 500 µL chloroform and mixed with 50 mg anhydrous BN. The Sb_{amo}-NP/BN mixture was then transferred into 1.5 mm thick quartz capillaries and sealed using epoxy resin to prevent oxidation while heating. Capillaries were placed flat on top of a ceramic heating plate and measurements were performed under constant heating ramp of 4 °C/min up to 400 °C with a temperature precision of ± 1 °C.

Scattering-Type Scanning Nearfield Optical Microscopy: To investigate the optical response of the crystalline and amorphous NP, a commercially available s-SNOM (NeaSNOM, neaspec GmbH) was used at frequencies of 900 and 1000 cm^{-1} with an LN2 cooled MCT-detector (Kolmar Technologies) to record the scattering amplitude, by lock-in detection of the light scattered from an AFM tip at higher harmonics of the tip oscillation frequency. The third demodulation order (S_3) is used here, as a good signal to noise ratio and a good background suppression are needed to separate the NP contributions from the background. The laser source used was a commercially available Quantum Cascade laser system (MIRcat, Daylight solution). The s-SNOM was operated at tapping frequencies of 220–270 kHz at tapping amplitudes of ca. 50 nm. The samples were prepared in an argon filled glovebox. Therefore, the sample was highly diluted in chloroform and treated by an ultrasonic finger with an amplitude set at 25 % for at least 2 min. Afterwards, the sample was drop-casted onto a silicon wafer and dried in the vacuum chamber of the glovebox. The sample was then transferred in an air-tight container to the measuring device even though the measurement itself was performed under atmosphere. Prior to storing the samples were transferred into a sputtering chamber with a base pressure of $3 \cdot 10^{-8}$ mbar. Nominally 15 nm $(ZnS)_{0.8}(SiO_2)_{0.2}$ capping is sputtered with an RF generator from a stoichiometric target at 65 W for 540 s, with an Ar pressure of $3.4 \cdot 10^{-2}$ mbar at room temperature.

X-Ray Photoelectron Spectroscopy: XPS was carried out in an AXIS Supra instrument (Kratos Analytical Ltd.) with a hemispherical analyzer. The spectrometer was calibrated with respect to the Ag $3d_{5/2}$ signal with a binding energy (BE) of 368.2 eV. During the measurements, the base pressure was $< 5.0 \cdot 10^{-6}$ Pa while a monochromatic Al K_α radiation was used, and a simultaneous charge neutralization (low-energy, electron-only source) was applied to compensate for charging effects. The size of the probed sample area was $700 \cdot 300$ µm^2. The intensity of detected photoelectrons was counteracted by applying a high emission current of 25 mA for both survey and high-resolution (Sb 3d, S 2p, I 3p, and C 1s) scans. During the measurement of the survey scans a pass energy of 160 eV and a step size of 0.25 eV was used (5 sweeps, dwell time = 100 ms), while a pass energy of 20 eV and a step size of 0.05 eV was applied for the high-resolution scans (20 sweeps, dwell time = 200 ms). The BE scale of all samples was calibrated with respect to the adventitious carbon signal at BE = 284.8 eV instead of using the fermi edge. The analysis of the spectra was performed in the CasaXPS software package (Casa Software Ltd.) by subtracting a Shirley background[58] sensitivity factors supplied by the instrument manufacturer for the quantification of the survey scans.

Supporting Information

Supporting Information is available from the Wiley Online Library or from the author.

Acknowledgements

This research was funded by the German Research Foundation (DFG, Bonn, Germany; Collaborative Research Center 917 "Nanoswitches"). The authors like to thank Prof. Joachim Mayer (Gemeinschaftslabor für Elektronenmikroskopie (GfE), RWTH Aachen) for the close collaboration, Eva Mayer and Peter Pollmann (Materials Chemistry (MCh), RWTH Aachen) for their assistance in XPS measurements, Anke Braun and Nina Nagel for their assistance in lab work and Tobias Storp for the collection of p-XRD data.

Open access funding enabled and organized by Projekt DEAL.

Conflict of Interest

The authors declare no conflict of interest.

Data Availability Statement

The data that support the findings of this study are available from the corresponding author upon reasonable request.

Keywords

antimony, nanoparticles, near-field optical microscopy, phase change materials

Received: March 21, 2024
Revised: June 30, 2024
Published online: July 11, 2024

[1] B. J. Shastri, A. N. Tait, T. Ferreira de Lima, W. H. Pernice, H. Bhaskaran, C. D. Wright, P. R. Prucnal, *Nat. Photonics* **2021**, *15*, 102.
[2] B. Sun, T. Guo, G. Zhou, S. Ranjan, Y. Jiao, L. Wei, Y. N. Zhou, Y. A. Wu, *Mater. Today Phys.* **2021**, *18*, 100393.
[3] M. S. Rahman, H. Reza, IEEE International Conference on Electro Information Technology (EIT), Chicago, IL, USA, August **2020**.
[4] Y. Hajjaji, W. Boulila, I. R. Farah, I. Romdhani, A. Hussain, *Comput. Sci. Rev.* **2021**, *39*, 100318.
[5] W. Zhang, R. Mazzarello, M. Wuttig, E. Ma, *Nat. Rev. Mater.* **2019**, *4*, 150.
[6] M. Galicia, S. Menzel, F. Merchant, M. Müller, H.-Y. Chen, Q.-T. Zhao, F. Cüppers, A. R. Jalil, Q. Shu, P. Schüffelgen, G. Mussler, C. Funck, C. Lanius, S. Wiefels, M. V. Witzleben, C. Bengel, N. Kopperberg, T. Ziegler, R. W. Ahmad, A. Krüger, L. Pöhls, R. Dittmann, S. Hoffmann-Eifert, V. Rana, D. Grützmacher, M. Wuttig, D. Wouters, A. Vescan, T. Gemmeke, J. Knoch, et al., Design, Automation & Test in Europe Conference & Exhibition, Antwerp, Belgium, March **2022**.
[7] M. Wuttig, N. Yamada, *Nat. Mater.* **2007**, *6*, 824.
[8] P. Prabhathan, K. V. Sreekanth, J. Teng, J. H. Ko, Y. J. Yoo, H. Jeong, Y. Lee, S. Zhang, T. Cao, C.-C. Popescu, B. Mills, T. Gu, Z. Fang, R. Chen, H. Tong, Y. Wang, Q. He, Y. Lu, Z. Liu, H. Yu, A. Mandal, Y. Cui, A. S. Ansari, V. Bhingardive, M. Kang, C. K. Lai, M. Merklein, M. J. Müller, Y. M. Song, Z. Tian, et al., *Iscience* **2023**, *26*, 107946.
[9] M. Le Gallo, A. Sebastian, *J. Phys. D: Appl. Phys.* **2020**, *53*, 213002.

[10] J. Hui, Q. Hu, H. Yuan, R. Shi, X. Huang, Y. Wu, Y. Ren, Z. Zhang, H. Wang, *Small* **2023**, *20*, 2307792.
[11] N. Bala, B. Khan, K. Singh, P. Singh, A. P. Singh, A. Thakur, *Mater. Adv.* **2023**, *4*, 747.
[12] A. Burtsev, N. Eliseev, V. Mikhalevsky, A. Kiselev, V. Ionin, V. Grebenev, D. Karimov, A. Lotin, *Mater. Sci. Semicond. Process.* **2022**, *150*, 106907.
[13] M. H. Lankhorst, B. W. Ketelaars, R. A. Wolters, *Nat. Mater.* **2005**, *4*, 347.
[14] Q. Xu, E. Lian, P. Yeoh, M. Skowronski, *AIP Adv.* **2022**, *12*, 065018.
[15] M. A. Luong, S. Ran, M. Bernard, A. Claverie, *Mater. Sci. Semicond. Process.* **2022**, *152*, 107101.
[16] M. Salinga, B. Kersting, I. Ronneberger, V. P. Jonnalagadda, X. T. Vu, M. Le Gallo, I. Giannopoulos, O. Cojocaru-Mirédin, R. Mazzarello, A. Sebastian, *Nat. Mater.* **2018**, *17*, 681.
[17] W. Hollemann, *Lehrbuch der Anorganischen Chemie 102. Auflage*, Walter de Gruyter, Berlin **2007**.
[18] X. Guo, Y. Hu, Q. Chou, T. Lai, X. Zhu, *J. Mater. Sci.: Mater. Electron.* **2018**, *29*, 16172.
[19] S. Aggarwal, T. Milne, N. Farmakidis, J. Feldmann, X. Li, Y. Shu, Z. Cheng, M. Salinga, W. H. Pernice, H. Bhaskaran, *Nano Lett.* **2022**, *22*, 3532.
[20] Z. Cheng, T. Milne, P. Salter, J. S. Kim, S. Humphrey, M. Boothand, H. Bhaskaran, *Sci. Adv.* **2021**, *7*, abd7097.
[21] D. T. Yimam, B. J. Kooi, *ACS Appl. Mater. Interfaces* **2022**, *14*, 13593.
[22] F. Jiao, B. Chen, K. Ding, K. Li, L. Wang, X. Zeng, F. Rao, *Appl. Mater. Today* **2020**, *20*, 100641.
[23] Y. Hu, Q. Qiu, X. Zhu, T. Lai, *Appl. Surf. Sci.* **2020**, *505*, 144337.
[24] Y. Z. Shen, H. Zhang, V. L. Deringer, R. Mazzarello, W. Zhang, *Nanoscale* **2023**, *15*, 15259.
[25] A. Frommelius, T. Ohlerth, M. Noyong, U. Simon, *Phys. Status Solidi* **2023**, 2300456.
[26] T. Saltzmann, M. Bornhöfft, J. Mayer, U. Simon, *Angew. Chem., Int. Ed.* **2015**, *54*, 6632.
[27] O. Yarema, A. Perevedentsev, V. Ovuka, P. Baade, S. Volk, V. Wood, M. Yarema, *Chem. Mater.* **2018**, *30*, 6134.
[28] C. N. Nanev, *J. Cryst. Growth* **2020**, *546*, 125786.
[29] M. He, K. Kravchyk, M. Walter, M. V. Kovalenko, *Nano Lett.* **2014**, *14*, 1255.
[30] M. G. Boebinger, O. Yarema, M. Yarema, K. A. Unocic, R. R. Unocic, V. Wood, M. T. McDowell, *Nat. Nanotechnol.* **2020**, *15*, 475.
[31] L. Balan, A. Dailly, R. Schneider, D. Billaud, P. Willmann, J. Olivier-Fourcade, J.-C. Jumas, *Hyperfine Interact.* **2005**, *165*, 101.
[32] A. Giannis, K. Sandhoff, *Angew. Chem., Int. Ed. Engl.* **1989**, *28*, 218.
[33] S. Mourdikoudis, M. Menelaou, N. Fiuza, G. Zheng, S. Wei, J. Perez-Juste, L. Polavarapu, Z. Sofer, *Nanoscale Horiz.* **2022**, *7*, 941.
[34] C. Barrett, P. Cucka, K. Haefner, *Acta Crystallogr.* **1963**, *16*, 451.
[35] P. Ballirano, A. Maras, *Z. Kristallog. – New Cryst. Struct.* **2002**, *217*, 177.
[36] F. Wang, R. Tang, H. Yu, P. C. Gibbons, W. E. Buhro, *Chem. Mater.* **2008**, *20*, 3656.
[37] V. N. Richards, S. P. Shields, W. E. Buhro, *Chem. Mater.* **2011**, *23*, 137.
[38] W. Huang, J. Zhu, M. Wang, L. Hu, Y. Tang, Y. Shu, Z. Xie, H. Zhang, *Adv. Funct. Mater.* **2021**, *31*, 2007584.
[39] K. P. Kepp, *Inorg. Chem.* **2016**, *55*, 9461.
[40] K. A. Hofmann, K. A. Hofmann, *Lehrbuch der anorganischen Experimentalchemie*, Vieweg+Teubner Verlag, Wiesbaden **1918**, p. 275–283.
[41] H. Schulz, *Chem. Texts* **2018**, *4*, 1.
[42] B. L. P. Bhattacharjee, *Chem. Soc. Rev.* **2023**, *52*, 2573.
[43] A. E. Whitten, B. Dittrich, M. A. Spackman, P. Turner, T. C. Brown, *Dalton Trans.* **2004**, *1*, 23.
[44] H. Watts, *Watts' Dictionary of Chemistry*, Longmans, Green and Co, New York **1894**.
[45] C. Wagner, A. Naumkin, A. Kraut-Vass, J. Allison, C. Powell, J. Rumble Jr, *National Institute of Standards and Technology*, Gaithersburg, MD **2003**, 20899.
[46] J. F. Moulder, W. F. Stickle, P. E. Sobol, K. D. Bomben, *Handbook of X-ray Photoelectron Spectroscopy*, Perkin-Elmer Corps, Waltham, MA **1992**.
[47] W. Liu, W. Yuen, R. Stradling, *J. Vac. Sci. Technol., B* **1995**, *13*, 1539.
[48] M. Wuttig, H. Bhaskaran, T. Taubner, *Nat. Photonics* **2017**, *11*, 465.
[49] J. Toudert, R. Serna, *Opt. Mater. Express* **2016**, *6*, 2434.
[50] Z. Cheng, T. Milne, P. Salter, J. S. Kim, S. Humphrey, M. Booth, H. Bhaskaran, *Sci. Adv.* **2021**, *7*, abd7097.
[51] J. M. Luther, P. K. Jain, T. Ewers, A. P. Alivisatos, *Nat. Mater.* **2011**, *10*, 361.
[52] F. Keilmann, R. Hillenbrand, *Proc. R. Soc. London, Ser. A* **2004**, *362*, 787.
[53] T. Taubner, F. Keilmann, R. Hillenbrand, *J. Korean Phys. Soc.* **2005**, *47*, 213.
[54] A. Cvitkovic, N. Ocelic, R. Hillenbrand, *Nano Lett.* **2007**, *7*, 3177.
[55] A. Cvitkovic, N. Ocelic, J. Aizpurua, R. Guckenberger, R. Hillenbrand, *Phys. Rev. Lett.* **2006**, *97*, 060801.
[56] J. Nishida, A. Otomo, T. Koitaya, A. Shiotari, T. Minato, R. Iino, T. Kumagai, *Nano Lett.* **2024**, *24*, 836.
[57] A. Nag, M. V. Kovalenko, J.-S. Lee, W. Liu, B. Spokoyny, D. V. Talapin, *J. Am. Chem. Soc.* **2011**, *133*, 10612.
[58] D. A. Shirley, *Phys. Rev. B* **1972**, *5*, 4709.